Modeling the Dynamic Variability of Sub-Relativistic Outer Radiation Belt Electron Fluxes Using Machine Learning

Donglai Ma[1] ⓘ, Xiangning Chu[2] ⓘ, Jacob Bortnik[1] ⓘ, Seth G. Claudepierre[1,3] ⓘ,
W. Kent Tobiska[4] ⓘ, Alfredo Cruz[4] ⓘ, S. Dave Bouwer[4], Joseph F. Fennell[3] ⓘ, and J. Bernard Blake[3] ⓘ

[1]Department of Atmospheric and Oceanic Sciences, University of California, Los Angeles, CA, USA, [2]Laboratory for Atmospheric and Space Physics, University of Colorado Boulder, Boulder, CO, USA, [3]Space Sciences Department, The Aerospace Corporation, El Segundo, CA, USA, [4]Space Environment Technologies, Pacific Palisades, CA, USA

Abstract We present a set of neural network models that reproduce the dynamics of electron fluxes in the range of 50 keV ~1 MeV in the outer radiation belt. The Outer Radiation belt Electron Neural net model for Medium energy electrons uses only solar wind conditions and geomagnetic indices as input. The models are trained on electron flux data from the Magnetic Electron Ion Spectrometer instrument onboard Van Allen Probes, and they can reproduce the dynamic variations of electron fluxes in different energy channels. The model results show high coefficient of determination ($R^2 \sim 0.78$–0.92) on the test data set, an out-of-sample 30-day period from 25 February to 25 March in 2017, when a geomagnetic storm took place, as well as an out-of-sample one year period after March 2018. In addition, the models are able to capture electron dynamics such as intensifications, decays, dropouts, and the Magnetic Local Time dependence of the lower energy ($\sim$<100 keV) electron fluxes during storms. The models have reliable prediction capability and can be used for a wide range of space weather applications. The general framework of building our model is not limited to radiation belt fluxes and could be used to build machine learning models for a variety of other plasma parameters in the Earth's magnetosphere.

Plain Language Summary The Earth's radiation belts consist of energetic particles trapped by the geomagnetic field. This radiation environment is known to be particularly hazardous to spacecrafts and difficult to predict given the complex dynamics of electrons at different energy states. This paper presents a set of neural-network-based models that use measurements of geomagnetic and solar activities as drivers to reconstruct radiation belt electron fluxes ranging from 50 keV to 1 MeV. The models can determine the flux with high accuracy and capture the electron dynamics with long- and short-term time scales. The models provide reliable prediction capability and can be used for a wide range of space weather applications. The approach through which our models are built is not limited to radiation belt fluxes and can be generalized for a variety of other plasma parameters in the Earth's magnetosphere.

1. Introduction

The Earth's energetic particle environment consists of electrons that range in energy from a few keV to multiple MeV (e.g., Baker et al., 2017; Thorne, 2010), and were discovered by Geiger counters flown on Explorer 1, launched in January 1958, which represents the first major discovery of the space age (Van Allen & Frank, 1959; Van Allen et al., 1958). The dynamics of the different electron energies that have been studied over several decades, but more recently in great detail facilitated by high quality data from the Van Allen Probes mission (Li & Hudson, 2019; Mauk et al., 2013). The exact response of the radiation belts to solar wind driving is difficult to predict due to various competing loss and acceleration processes, often giving vastly different responses to seemingly similar driving conditions (Reeves et al., 2003) but occasionally even being accelerated up to roughly 10 MeV. The generally accepted process of radiation belt flux enhancement is believed to proceed as follows: an increase in the strength of the convection electric field causes an enhanced drift of plasma-sheet electrons into the inner magnetosphere, where they gradient-drift eastwards, and become unstable to plasma wave excitation. A particular class of waves, called whistler-mode chorus waves is excited on the dawn side of the Earth by ~10–100 keV "source" electrons, and these waves then transfer a portion of their energy to higher energy "seed" electrons (>100 keV), that are further accelerated to relativistic energies (~MeV) facilitated by Ultra-Low Frequency waves (Bortnik & Thorne, 2007; Li & Hudson, 2019; Li et al., 2006; Reeves et al., 2003; Thorne et al., 2013; Turner et al., 2013; Xiao et al., 2009).

In addition, the energy-dependent dynamics of radiation belt electrons at multiple energies can operate on different time scales and have vastly different behaviors (e.g., Ma et al., 2016; Reeves et al., 2016). For example, the Van Allen Probes were able to identify an "impenetrable" barrier to relativistic electron inward motion (Baker et al., 2014) at L ∼ 2.8, while lower energy electrons exhibit fast dynamics and are more likely to fill the slot region and penetrate into the inner zone (Reeves et al., 2016). Besides, more enhancement events occur at lower energies compared to higher energies while the lifetime of the former is much shorter than the latter in the outer radiation belt (Claudepierre et al., 2020a, 2020b; Reeves et al., 2016). Thus, developing useful models to describe the trapped electron flux across a range of different energy channels is important for understanding and predicting the dynamics and distribution of the radiation belts.

The outer radiation belt electron fluxes and their dynamics have been modeled using a variety of approaches including both data-driven and physics-based models. The empirical AE8 and AE9 models are statistical models which are static, and reconstruct the distribution of electrons from 40 keV to 7 MeV (Ginet et al., 2013; Sawyer & Vette, 1976). Other statistical models such as CRRESELE (Brautigam & Bell, 1995) covers 500 keV ∼ 6.6 MeV, the IGE-2006 (Sicard-Piet et al., 2008) and the POLE (Sicard-Piet et al., 2006) are applicable only for geostationary orbit, whereas the FLUMIC (Wrenn et al., 2000) and the MODE-DIC model (Hands et al., 2015) model the worst case scenario for 1-day fluence and environment for spacecraft internal charging. These empirical models depend on L shell and energy but are usually independent of geomagnetic activity, meaning that they are static, that is, they reproduce "statistically averaged" conditions. Several machine learning models have also been developed to study trapped electron fluxes in the radiation belts. These include Balikhin et al. (2011) who used the Nonlinear Autoregressive Moving Average with Exogenous inputs approach, and Zhang et al. (2020) who used Artificial Neural Networks (ANNs) with quantile regression. Both models focus on the fluxes at geosynchoronous (GEO) orbit. Smirnov et al. (2020) adopted a gradient boosting decision tree method on GPS data to model the fluxes of electrons with energies in the range 120–600 keV in the MEO region which only captures one altitude. Lima et al. (2020) used a combination of data collected at low earth orbit and LANL-01A at GEO orbit and POES electron fluxes as the input of the model to predict MeV energy flux and Claudepierre and O'Brien (2020) also included POES data from LEO as the driver of their neural network model, which operates on a daily cadence.

Using physics-based models is another important way to replicate and understand the dynamic behavior of the radiation belts. One common method is through the integration of the Fokker-Planck (FP) equation (Glauert et al., 2014; Lyons & Thorne, 1973; Ma et al., 2015; Reeves et al., 2012a; Tu et al., 2013). However, the FP model can only represent the effects of diffusive scattering on the particles, it cannot represent nonlinear processes, nor include any unknown (or unquantified physical process which might shift the balance between acceleration and loss processes). And such physical-based modeling requires artificial or observed initial and boundary conditions to drive the simulation which also need to be specified during the course of the simulation.

Here, we present a novel strategy based on the ANN model to overcome some of these shortcomings. This approach is versatile and can be applied to a variety of physical quantities sampled at sparse locations and times, and has already been utilized in space weather modeling the plasma density, chorus and hiss waves, and in conjunction with physics-based radiation belt modeling (Bortnik et al., 2016; Bortnik et al., 2018; Chu, Bortnik, Li, Ma, Angelopoulos, & Thorne, 2017; Chu, Bortnik, Li, Ma, Denton, et al., 2017; Chu et al., 2021). We describe and demonstrate the development of several ANN models of outer radiation belt electron fluxes covering energy channels from ∼50 keV to ∼1 MeV based on Van Allen Probes data. Since solar wind driving and geomagnetic activity alone determine the fluctuation of the outer radiation belt, the neural network model accepts these parameters as inputs without relying on any boundary conditions from other satellite data, making this model a tool with great potential in predicting and understanding radiation belt dynamics. We show that our electron flux model captures the dominant features of the variability at different time scales, as well as the energy-dependent dynamics and the MLT dependence of the low energy channel.

2. Data Description

2.1. MagEIS Electron Flux Data

The primary data used throughout this work are obtained from the Magnetic Electron Ion Spectrometer (MagEIS) instrument suite (Blake et al., 2013) onboard NASA's Van Allen Probes (Mauk et al., 2013). The identically instrumented twin-spacecraft Van Allen Probes mission has a highly elliptical low-inclination orbit with an
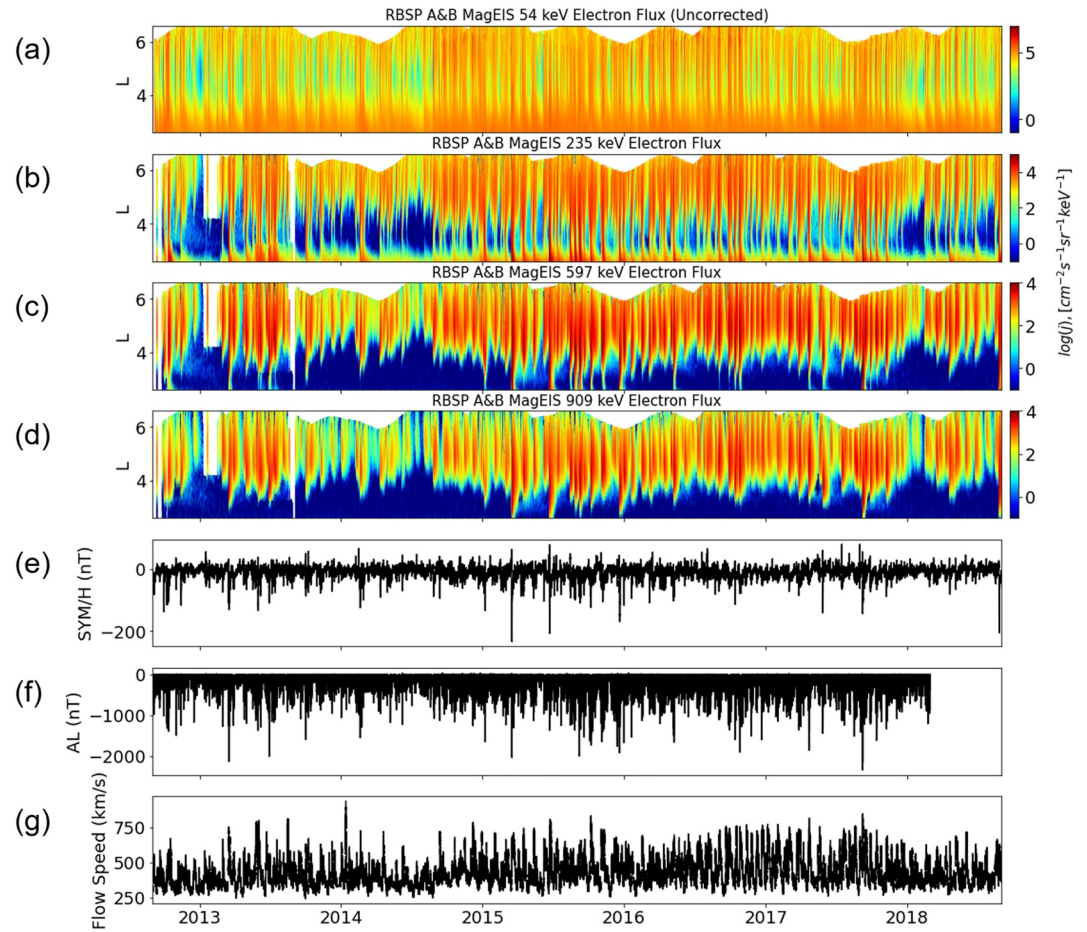
Figure 1. (a–d) Spin-Averaged fluxes of electrons with energies of 54, 235, 597, 909 keV from Magnetic Electron Ion Spectrometer (MagEIS) on RBSP A and B for the indicated time interval. The MagEIS fluxes reflect uncorrected data for channel 54 keV and corrected data for the remaining channels (e–g) 5-min resolution SYM-H and AL indices and solar wind speed from the OMNI data set.

apogee of $\sim 6R_E$ and a perigee of ~ 600 km. The MagEIS instruments measure electron fluxes throughout this orbit over a wide energy range (~ 30–4 MeV) with four electron spectrometers (LOW: ~ 30–200 keV, M75, and M35: ~ 200 keV to 1 MeV, HIGH: 1–4 MeV). The current study illustrates the capabilities of the machine learning model using four selected energy channels from the MagEIS instrument (54 keV, 235 keV, 597 keV, and 909 keV shown in Figure 1). Extensive background correction of MagEIS spin-averaged fluxes was performed to remove background contamination due to inner belt protons and high energy electrons that produce bremsstrahlung X rays (Claudepierre et al., 2015, 2019). However, there are periods when the background correction cannot be performed, and as a result, background corrected MagEIS data at energies $<\sim 220$ keV is only available at L > 4 on RBSP-B. For lower energy electron fluxes, the drift period is relatively long. Thus the data available on both probes are preferentially used in our study in order to capture the magnetic local time (MLT) dependence. For the above reasons, we use uncorrected data on 54 keV channel and background corrected data on other three channels.

The temporal resolution of the data is reduced to 5 min averages, and the L shell is restricted to L > 2.6 to focus on the dynamic variability in the outer radiation belt, which results in a data set containing ~ 1 million data points in each energy channel.

2.2. OMNI Data Set

The variation of the Earth's outer radiation belt is known to be driven by the solar wind (e.g., solar wind pressure leading to magnetopause shadowing, inward convection of plasma from the tail, and creation of ultralow frequency waves facilitating radial diffusion) and the resultant geomagnetic activity (e.g., whistler-mode chorus and hiss waves induced by the plasma injections from the magnetotail). Therefore, the neural network model uses both solar wind parameters as well as geomagnetic indices acquired from the OMNI data set (https://omniweb.gsfc.nasa.gov/) as input parameters (5-min resolution). It is important to use both because occasionally structures observed in the solar wind can miss the Earth resulting in minimal geomagnetic activity, or vice versa, so using both solar wind parameters and geomagnetic indices reflects both fundamental drivers and their geoeffectiveness (Walsh et al., 2019). The OMNI AL and AE indices end after 1 March 2018, so the electron flux data used in the model training process is from October 2012 to February 2018. The candidate input parameters include AE, AL, AU, ASY-D, ASY-H, Bz-GSM, E, flow speed, solar wind pressure, proton density, SYM-H, and SYM-D.

3. Methodology

3.1. Model Description

We use a simple fully connected Multi-Layer Perceptron model to reconstruct the energetic electron fluxes from a number of different channels throughout the outer radiation belt. The approach represents an extension of the technique used in a number of previous studies, which successfully modeled plasma density, waves, and electron fluxes (Bortnik et al., 2016; Bortnik et al., 2018; Chu, Bortnik, Li, Ma, Angelopoulos, & Thorne, 2017; Chu, Bortnik, Li, Ma, Denton, et al., 2017). The input parameters used for each neuron in layer l are the products of the output of the preceding layer's $(l-1)$ nodes with their associated weights

$$z_j^l = f\left(\sum_{i=0}^{N-1} z_i^{l-1} w_{ij} + b_i\right) \tag{1}$$

where i and j denote the neuron number in the preceding $(l-1)$ and current (l) layers, respectively, and w_{ij} and b_i are the weights and biases in the hidden layer. The output of each neuron in the hidden layers is calculated using a RELU activation function

$$f\left(z^l\right) = \max\left(0, z^l\right) \tag{2}$$

which is one of the most widely used activation functions in deep learning (LeCun et al., 2015; Nair & Hinton, 2010). After each hidden layer, we place a batch normalization layer to prevent the vanishing and exploding gradient problem (Ioffe & Szegedy, 2015).

The outputs of the preceding $(l-1)$ layer's neurons are all used as the inputs of the neurons in the next layer (l), thus creating a fully connected feedforward neural network. Since the corrected MagEIS electron fluxes has many zero values, the model takes the function $log_{10}(flux + 1)$ as its output, where the 1 is added to avoid taking the log of zero, but does not affect the flux value otherwise since flux values typically take on large values $\sim 10^4 - 10^6$ as shown in Figure 1. The model is trained using the Nesterov-accelerated Adaptive Moment Estimation (Nadam) optimizer with default settings in Tensorflow (https://www.tensorflow.org/api_docs/python/tf/keras/optimizers/Nadam) to minimize the mean squared error (MSE) of the output. The dropout and early stopping methods are used in the same way in previous studies (Bortnik et al., 2016; Bortnik et al., 2018; Chu, Bortnik, Li, Ma, Angelopoulos, & Thorne, 2017; Chu, Bortnik, Li, Ma, Denton, et al., 2017; Chu et al., 2021).

The whole data set of electron flux measurements from RBSP A and B (October 2012–April 2019) was split into three distinct subsets: Part 1: One-year interval between March 2018 and April 2019 when the AL and AE indices from the OMNI data set were not available; Part 2: One-month interval between 25 February and 25 March 2017, when a geomagnetic storm occurred; Part 3: Remaining data. We used Part 3 to train, validate and test the model. Part 1 and Part 2 were only used to evaluate the model's true out-of-sample performance. The Part 3 was further split into 2-day segments. The 2-day segment length was chosen so that it would be much larger than the time resolution of the electron fluxes and input parameters, to ensure that the data samples that are close in time will not be correlated between testing and training sets, and it would be much smaller than the whole period of five years to ensure a large number of time chunks and that target flux data in the testing and training sets were

Table 1
Selected Lengths of Time History t_h, Time Resolution t_0 and Parameters Q_k at Different Channels

Channel	t_0	Best t_h	Q_k
54 keV	30 min	4 days	AE, SYM-H, Psw, Vsw
235 keV	60 min	10 days	AL, Psw, SYM-H, Vsw
597 keV	90 min	14 days	AL, SYM-H, Psw, Vsw
909 keV	120 min	18 days	AL, SYM-H, Vsw, Psw

distributed similarly. It is worth noting that in each 2-day interval, both RBSP A and B observations are merged together from the outset and then divided into separate data segments. Therefore, we ensure that the observations of RBSP A and B from the same time intervals will be retained together in either the training or test data set, will never appear in both, in order to avoid data leakage.

The training process of the final model includes two stages: Stage 1: Input parameter selection. In this stage, we use a five-fold cross-validation method, a subsample of 20% segments are retained as the validation data for testing the model, and the remaining four subsamples are used as training data. The cross-validation process is then repeated five times, with each of the five subsamples used exactly once as the validation data to get the most accurate quantification of the errors. The detailed process of input parameters selection is described in Section 3.2; Stage 2: Hyperparameter optimization for a best model. After we determine the input parameters, we optimize the hyperparameters to obtain a best final model, with 70% of segments used for the training set, 15% for the validation set and 15% is set side as the test set to evaluate the model performance. The training process uses the training data set to update the weights and biases, and its performance is assessed on the validation data set. When the MSE of the validation set stops improving for several steps in a row (eight steps in this study), the training process ends to avoid overfitting and ensure maximum generalizability to unseen data.

3.2. Input Parameters Selection and Hyperparameters Tuning

Our ANN models can be described as $F_i(\mathbf{X}(t); \mathbf{Q}_{1i}, \mathbf{Q}_{2i}, \ldots, \mathbf{Q}_{ki})$, where i denotes the energy channel being modeled, k denotes the selected different input indices, and $\mathbf{X}(t)$ represents the position of the spacecraft at the time of observation, using the vector $(L, \sin(MLT), \cos(MLT), MLAT)$. The reason for using trigonometric functions for the azimuthal coordinate is to eliminate the discontinuity at $MLT = 0$. The $\mathbf{Q}_{ki}(t, t_{0i}, t_{hi})$ is time series of time-averaged candidate solar wind parameters or geomagnetic indices with resolution t_{0i} and time history of length t_{hi}. The set of time resolution values t_0 for the 909 keV channel was based on our previous 1.8 MeV model (Chu et al., 2021) and decreasing with energy based on the different characteristic dynamic time scales. The initial t_h is based on the electron lifetime observed by Claudepierre et al. (2020b) for different channels and is further tuned in the following step.

The feature selection technique utilized here is essentially focused on adding the most informative predictors to the model sequentially (Kuhn and Johnson, 2013) and evaluating its performance. First, We select a 3-hidden-layer neural network model with 500, 100, and 10 neurons respectively, and with 0.2 drop rate for each layer as a base model. The model size selection is based on our total sample size and previous study experience. We loop through the candidate $\mathbf{Q}$ in Section 2.2 as input and evaluate the test performance using group 5-fold cross-validation. After we iterate through all the input parameters $\mathbf{Q}$, we select the time series with best performance (e.g., AL), and then combine that $\mathbf{Q}_{best}$ with another $\mathbf{Q}$ to repeat the iteration process. Finally, we stop the iteration when $k = 4$ for all the channels due to consistency and the test results that improvements of R^2 score value at $k = 5$ are small (less than 0.01). The specified parameters $\mathbf{Q}_k$ for each channel are shown in Table 1 in decreasing order of importance. The fact that final parameters include solar wind speed (V_{sw}), pressure (P_{sw}), SYM-H and auroral electrojet (AE or AL) index is consistent with our physical understanding of the processes involved and a large number of previous studies (e.g., Baker et al., 1979; Baker et al., 2014; Wing et al., 2016, 2022).

We then studied the model performance at various time periods to discover the ideal length t_h for the time series of input parameters. Figure 2 (left) plots the median and standard deviation of the test performance based on the group 5-fold cross-validation, while the right panel shows those of the coefficient of determination, denoted as R-squared. The best t_h values determined for each channel are shown in Table 1. They are considerably longer than the estimated electron lifetime in the outer radiation belt for the corresponding energy (Claudepierre et al., 2020a, 2020b), which suggests that dynamics with time scales smaller than simple decay would be captured in the input time series. After we determined the input parameters, we retrain the models as described in Section 3.1 Stage 2. The hyperparameters of the ORIENT-M models, including the number of hidden layers, the number of neurons in each hidden layer and the dropout rates, are optimized using a Tree-structured Parzen estimator algorithm (Bergstra et al., 2011, 2013) implemented in Optuna (Akiba et al., 2019). The final models'
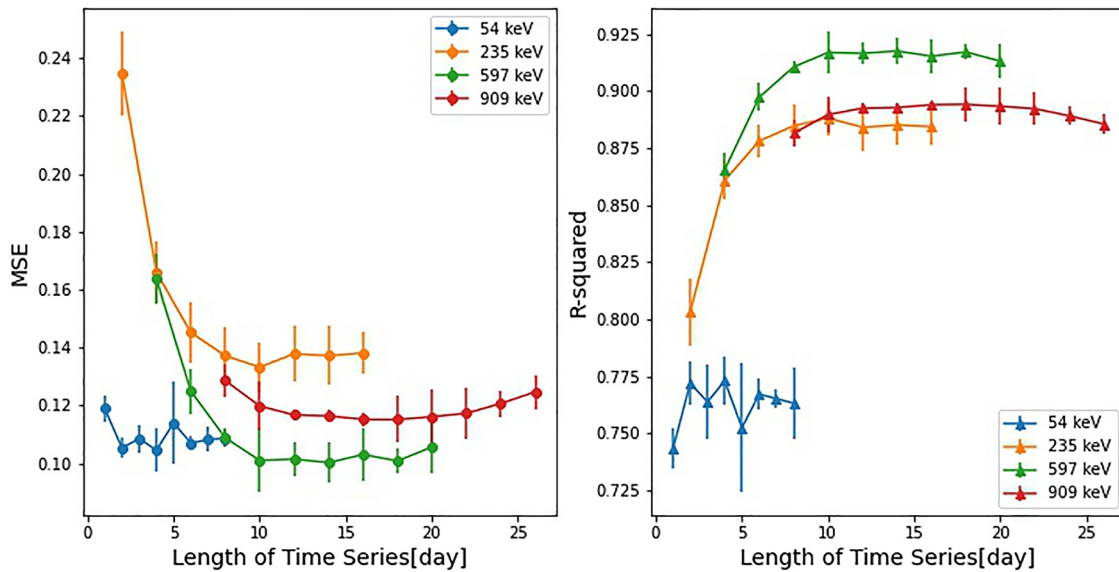
Figure 2. Model performance on the test data set using different lengths of time series as input parameters for each channel. The error bars show the median and standard deviation of mean squared error (left panel) and coefficient of determination R-squared.

structure and Optuna's hyperparameter search space are shown in Table S1 in Supporting Information S1. We are aware of the limitations that the tuning process of the hyperparameters should be performed at once, including the time-lags of the input parameters, the hyperparameters of the neural networks and etc. However, the number of hyperparameters are so large that the search space of hyperparameters is huge and will require a very large amount of computation power. Therefore, the workflow has been adapted as described above to save computation time. A complementary method which could help this complicated parameter selection problem is using information theory to investigate the information transfer from one parameter to another and the response lag time (e.g., Wing et al., 2016; Wing et al., 2022).

4. Model Results

A popular metric widely used in machine learning is the R^2 score. This indicator is used to quantify the fraction of variance explained by the model. It provides an indication of goodness of fit and therefore a measure of how well unseen samples are likely to be predicted by the model, through the proportion of explained variance. If $\hat{y}$ is the predicted value of the ith sample and y_i is the corresponding true value for total n samples, the estimated R^2 is defined as:

$$R^2(y, \hat{y}) = 1 - \frac{\sum_{i=1}^{n} (y_i - \hat{y}_i)^2}{\sum_{i=1}^{n} (y_i - \bar{y})^2}$$

where $\bar{y} = \frac{1}{n} \sum_{i=1}^{n} y_i$ and this R^2 score is the same with prediction efficiency, PE, described in Reeves et al. (2012b).

Figures 3 and 4 show a comparison between the observations and model results for two energy channels (235 and 597 keV) for the out-of-sample one month period between 25 February 2017, and 25 March 2017, during which a moderate geomagnetic storm (Dst minimum −74 nT) occurred. The geomagnetic indices (SYM-H and AE), the solar wind dynamic pressure (P_{sw}), and flow speed (V_{sw}) are shown in panels a and b. A strong interplanetary shock arrived at 9 UT on 1 March 2017, as indicated by the substantial and sudden increase (denoted by the vertical dashed line) in solar wind velocity and solar wind dynamic pressure.

Figures 3c and 3d show a comparison between the observed and modeled 235 keV electron fluxes as functions of time and L shell along the satellite trajectory, showing very close agreement at almost all times. Figure 3g shows the modeled 235 keV electron fluxes on the equatorial plane (MLAT = 0°, MLT = 0), highlighting the ANN model's utility in reconstructing electron flux data based on geomagnetic indices and solar wind parameters alone.
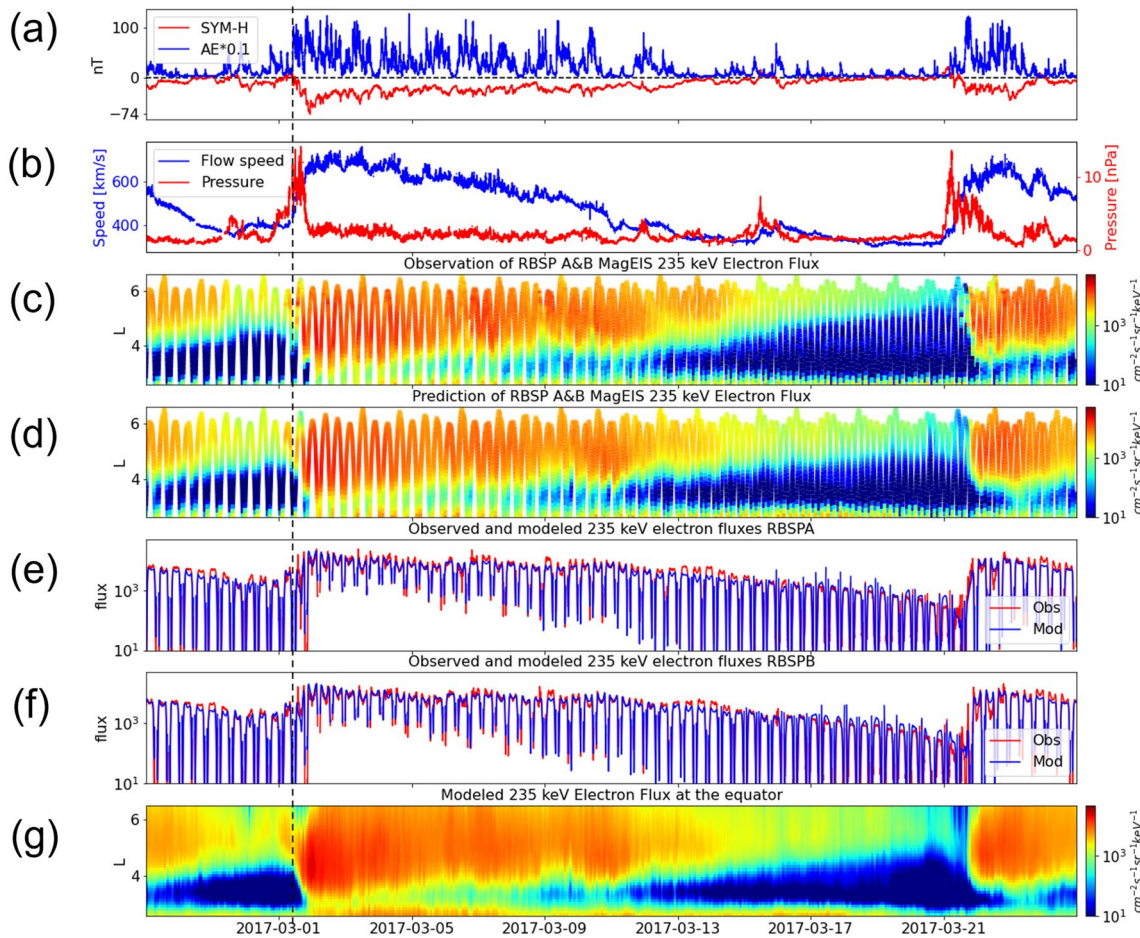
Figure 3. An example of the 235 keV model results during the month-long period between 25 February 2017, and 25 March 2017, which was held out from the training set for test purposes. (a) Geomagnetic indices SYM-H and AL; (b) The solar wind flow speed (V_{sw}) and dynamic pressure (P_{sw}) (c)–(d) the observed and modeled 235 keV electron fluxes as a function of L shell and time (e)–(f) the observed and modeled 235 keV electron fluxes along the trajectories of Van Allen Probe A and B; (g) the modeled 235 keV electron fluxes on the equatorial plane.

Figures 4c,4d and 4g show the same analysis but for 597 keV electron fluxes. Again, the models are seen to accurately reproduce the general variation of the electron fluxes as well as several key aspects of the general radiation belt behavior, including the effects of physical processes such as rapid local acceleration, radial diffusion, and flux decay. In addition, the comparison of Figure 3 and Figure 4 clearly shows the capabilities of our model in reconstructing the energy-dependent dynamics of the outer radiation belt.

The analysis in Figures 3 and 4 shows that each model is able to capture the rapid electron flux enhancement at 2017-03-01 UT and shows excellent agreement in the peak value of the flux and its location. The model-reproduced enhancement first occurs in the 235 keV channel and is later visible in the 597 keV channel, which demonstrates that the low energy seed population is gradually accelerated, most likely due to wave-particle interactions as has been suggested previously (Horne et al., 2003; Jaynes et al., 2015; Li et al., 2014), consistent with observations. In addition, at 235 keV, the electron fluxes in this enhancement event are seen to fill the slot region and penetrate into the inner zone, showing that the enhancement of electrons of the inner zone is also well captured. At 597 keV and 909 keV (Figure S1), the electron fluxes do not penetrate into the lower L shells, and the ANN model reproduces the "impenetrable barrier" precisely, implicitly "baking in" all the relevant physical processes into the model that prevent further penetration of these electrons to lower L-shells (Baker et al., 2014; Reeves et al., 2016). Last, the slow decay of the electron fluxes is well captured. Interestingly, the models successfully reproduce the timing, L-shell, and energy dependence of this decay process. From March 14, the flux decayed more rapidly at $4.0 < L < 4.5$ for the 235 keV channel electrons than it did for 597 keV electrons consistent with
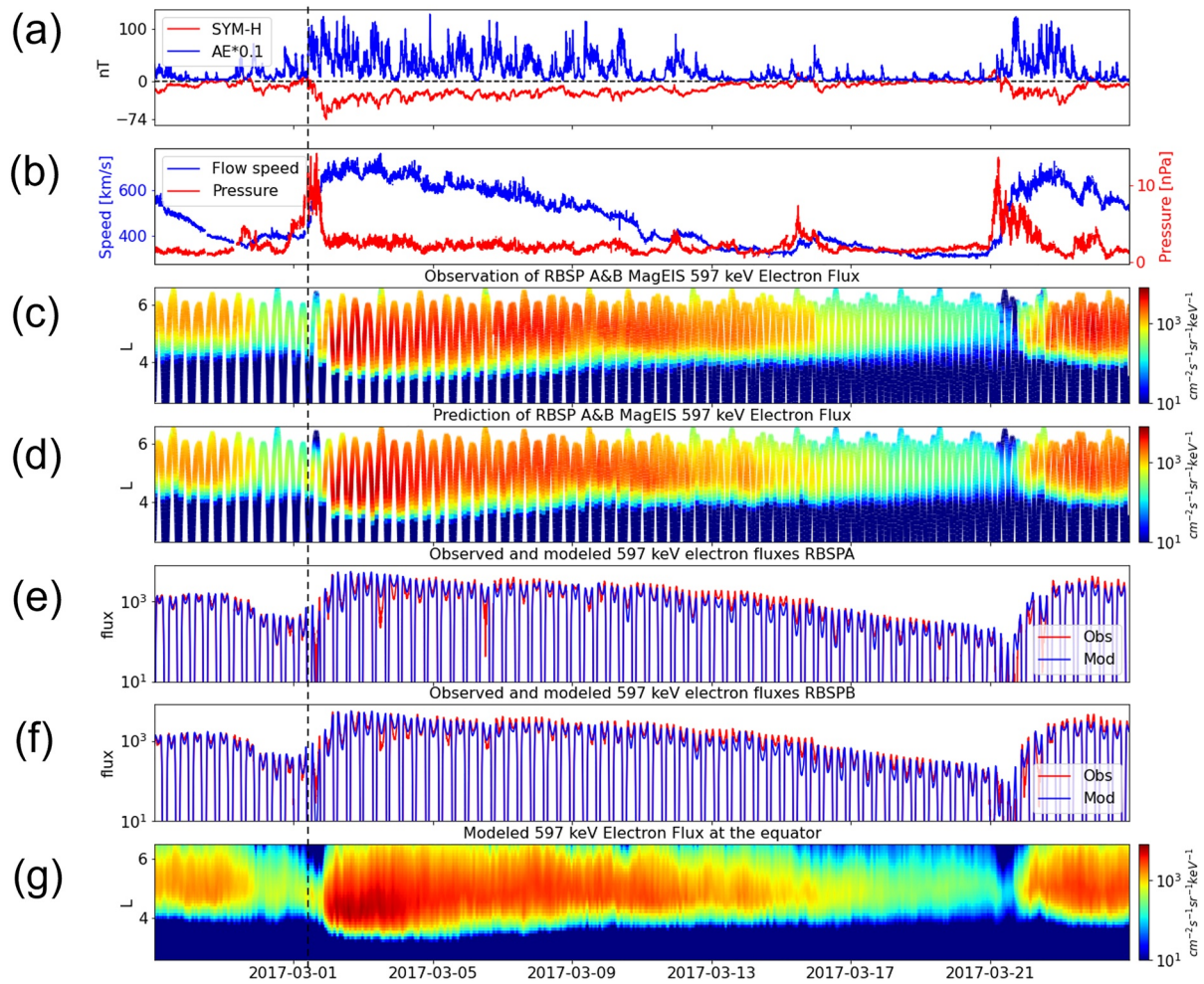
Figure 4. Similar to Figure 3, but for the 597 keV electron fluxes.

previous observations and theoretical estimates of electron lifetimes. Similar features are also observed before March 1 (Claudepierre et al., 2020a, 2020b; Reeves et al., 2016).

Figures 3e and 3f show the comparison between the observed (red) and modeled electron fluxes along the RBSP-A and RBSP-B trajectories, and a similar analysis is shown for the 597 keV electron fluxes in Figures 4e and 4f. Based on this comparison, the overall R-squared value of those two channels for the out-of-sample period are calculated to be 0.91 (235 keV) and 0.96 (597 keV) and the mean-squared error (MSE) between model results and observations are 0.10 (235 keV) and 0.05 (597 keV). The out-of-sample performance metrics are consistent with the performance of Part 3 test data set analysis shown in Figure 5. These results indicate that the models can predict the (sequentially organized) out-of-sample data with a 90% cross-correlation (i.e., variability of the response data around its mean) and a factor of ~2 performance in those channels which are comparable to the instrument accuracy. The performance of the 54 keV electron fluxes is not as good as the higher energy channels, as expected due to its complicated and rapid dynamics, as well as consisting of uncorrected data, which may add uncertainty to observed flux values. But the result in the out-of-sample period and test data set ($R^2 \sim$ 0.8) are still satisfactory and capture the important dynamics (See Figure S1).

Figures 6 and 7(a-c) show comparisons between the observed and modeled 235 and 597 keV electron fluxes along the trajectories of RBSP A and B between 1 March 2018 and 1 April 2019. It is important to note that here we are using predicted AL index since the observed OMNI AL index is not available after March 2018. Because the electron fluxes during this time period were not included in the training process (Section 3.2), the comparisons demonstrate the models' out-of-sample predictive ability. The predicted AL index using upstream solar
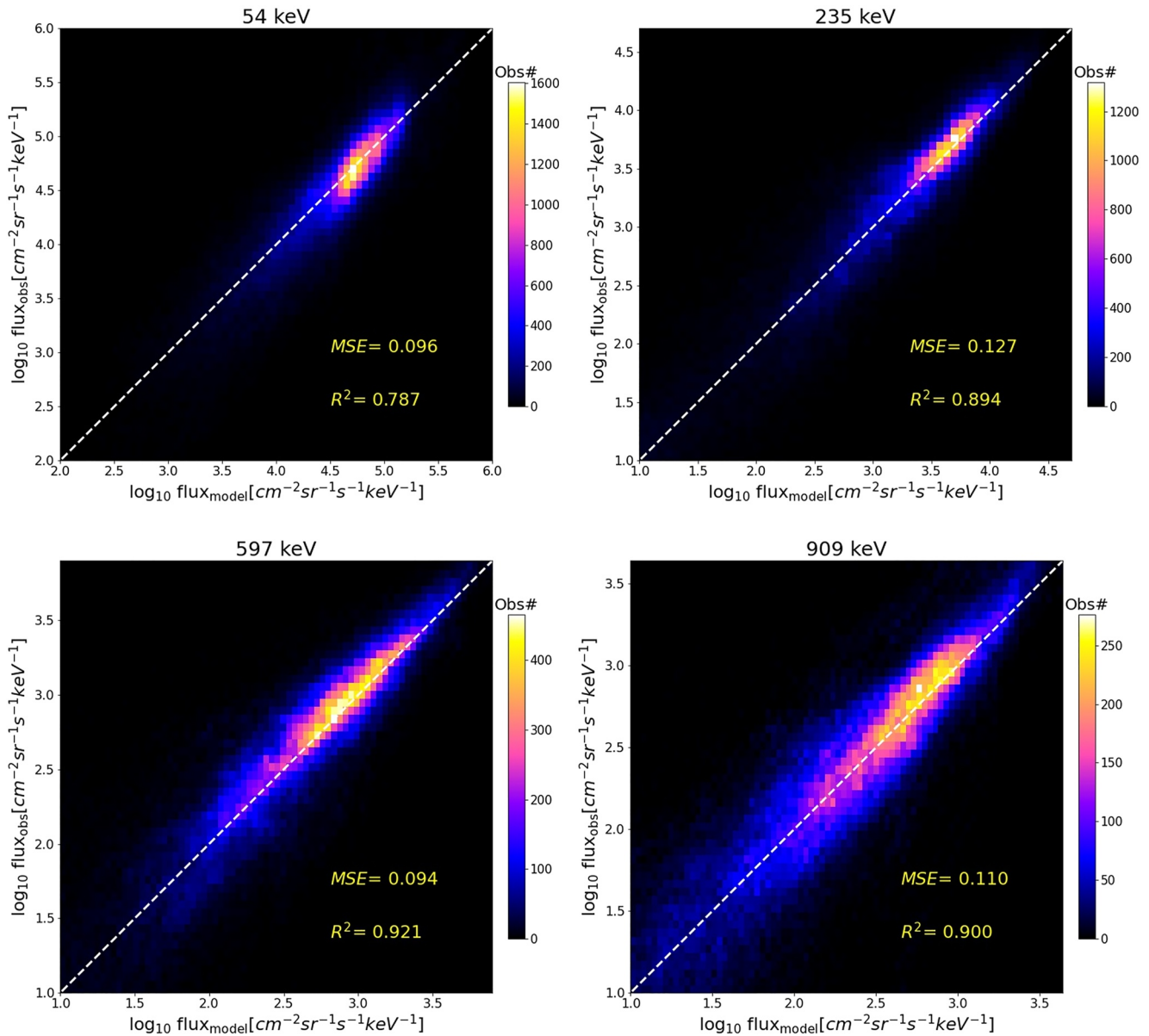
Figure 5. Model performance on the test data set of Part 3 for different electron energy channels (a–d) test data at 54, 235, 597, and 909 keV. The white dashed lines are diagonal lines that indicate perfect agreement (y = x) between the observations and model results. The coefficient of determination R-squared and mean squared error are shown at the right bottom corners.

wind measurements is available at lasp.colorado.edu/home/personnel/xinlin.li (Li et al., 2007; Luo et al., 2013), which has a linear correlation coefficient of 0.846 and a prediction efficiency of 0.715. The errors, as shown in Figures 6c and 7c, are defined as the difference between the training target of observed and modeled electron fluxes: $log_{10} (flux_{obs} + 1) - log_{10} (flux_{model} + 1)$. The results show that our models can reproduce rich dynamics in the fluxes, with rapid enhancements penetrating through the slot region into the inner zone. In particular, the models capture the rapid enhancement and penetration depth during the strong storm on 26 August 2018. The R-squared value of those two channels for the out-of-sample period along the orbit are calculated to be 0.80 (235 keV) and 0.87 (597 keV) and the MSE between model results and observations are 0.2 (235 keV) and 0.15 (597 keV). We emphasize that the errors originate from both the error in the predicted AL index and from our models. Figures 6 and 7d show the RBSP-A observations and the ORIENT-M output for L around 5.2 (select data from 5.1 < L < 5.3). The R^2 scores between the two are 0.71 (235 keV) and 0.77 (597 keV). One can therefore conclude that the ORIENT-M model generalizes well on the unseen data, both at a fixed L and along the orbit.
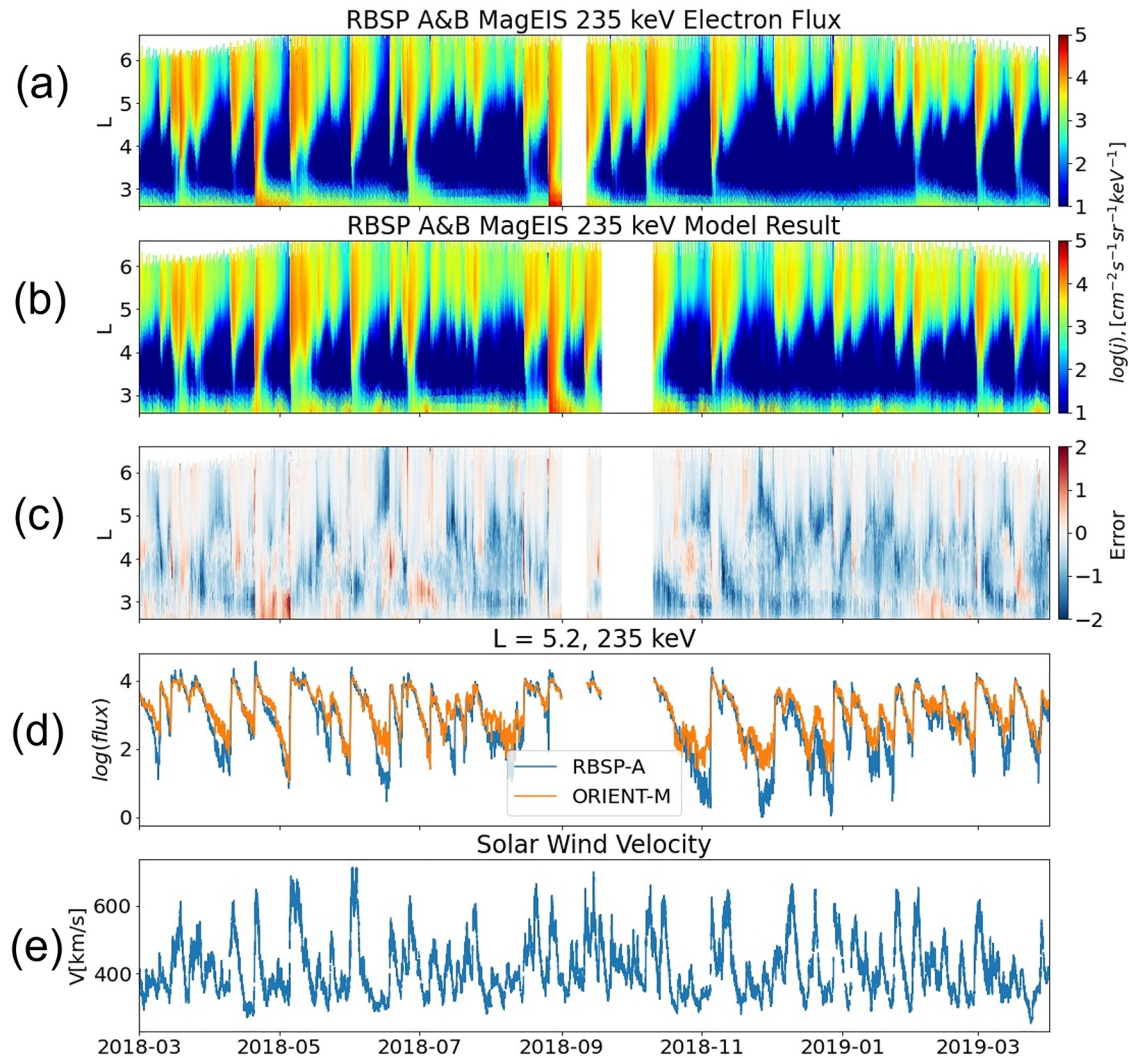
Figure 6. Out-of-sample model results produced along the Van Allen Probes' trajectories after March 2018 using the predicted AL index (lasp.colorado.edu/home/personnel/xinlin.li) as input while the other inputs are obtained from the OMNI database. (a) The observed 235 keV electron fluxes along the trajectories of Van Allen Probes. (b) The 235 keV model results along the trajectories. (c) The differences between the observed and modeled electron fluxes, which are defined as log_{10} $(flux_{obs} + 1) - log_{10}(flux_{model} + 1)$. (d) Comparison of observed and predicted flux at the fixed L-shell of 5.2 (e) solar wind velocity The white gap in panel (a) is due to missing data on the RBSP data website (https://rbsp-ect.lanl.gov/rbsp_ect.php). The gap in panel (b) is due to a 10-day gap in the predicted AL index.

The R^2 values of the four channels' test datasets for different L-shells and MLTs are shown in Figure 9. It is shown clearly that except the margin regions, our models can produce good results. The 54 keV model performance of the inner zone, which extends to higher L shell for low energy flux, is not as good as the outer zone. A possible explanation may be that the dynamics of inner zone are much less than that of the outer zone and our model cannot capture it accurately. For the regions with low R^2 value of 597 keV ($L \sim 3$, MLT from 6 to 8) and 909 keV ($L \sim 3$, MLT from 4 to 8), the samples in the test data set are only composed of very low flux measurements ($flux < 10 \ [cm^{-2}sr^{-1}s^{-1} \ keV^{-1}]$) so that these discrepancies can be negligible.

Since the velocity of the electron drift motion around the Earth is energy-dependent, the global electron distribution following storms and substorms is expected to show an energy-related variation in MLT. This energy-dependent distribution results from a competition of the electron drift period and the loss timescale for that particular energy of electrons. For relativistic electrons ($\sim$MeV), the drift period is very small (tens of minutes) and the loss times-cale is large (several days), so the drift motion dominates, and the fluxes are almost symmetrical in MLT about the Earth. However, at lower electron energies (tens to a few hundred keV), the energy-dependent magnetic drifts
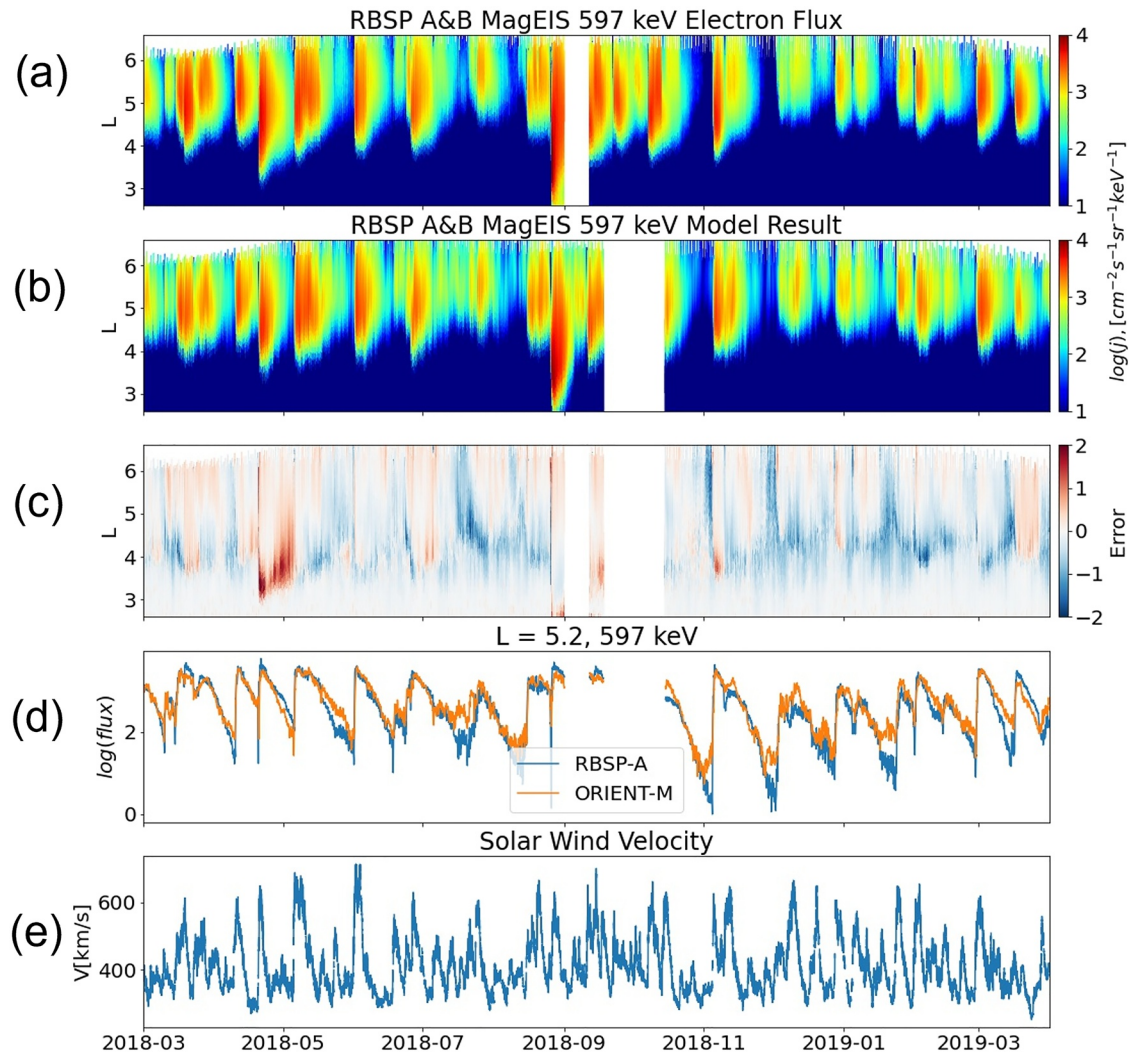
Figure 7. Similar to Figure 6, but for the 597 keV electron fluxes.

are far slower, the drift periods are longer, and the loss timescales are shorter, such that the electron fluxes can vary dramatically within a limited range of MLTs.

Figure 8 shows the modeled equatorial electron flux distribution variation for 54 keV, 235 keV, and 597 keV (A2, B2, C2) and the corresponding RBSP observations (A1, B1, C1) during a geomagnetic storm that occurred on 8 April 2016. The ORIENT-M model results show the distribution of L-shell and MLT, which exhibit different dynamics for each energy channel. Before the storm (time a), the electron fluxes at each energy channel are seen to be approximately symmetric in MLT. However, when the storm begins (time b), there is an observed enhancement for the 54 keV electrons at the Earth's dawnside consistent with plasmasheet electrons being convected from the tail and drifting Eastwards due to magnetic gradients. In contrast, the higher energy channels exhibit a dropout in fluxes that has a roughly MLT-symmetric distribution. At the peak of the geomagnetic activity (as measured by a minimum in the AL index) the 54 keV electron fluxes (time c) show significant MLT asymmetry in the electron flux enhancements, which is observed predominantly at $L \sim 3 - 6$, and is a reflection of the eastward drift of electrons around the Earth, as well as the rapid loss processes (e.g., scattering by chorus waves) that remove the majority of the enhanced electron fluxes as they drift from the day through to the dusk sectors (See Figures 8 54 keV (d) and Movie S1). It is worth mentioning that the result of Figure 8 cannot be verified at every MLT since we only have two satellites that cannot be everywhere present simultaneously.
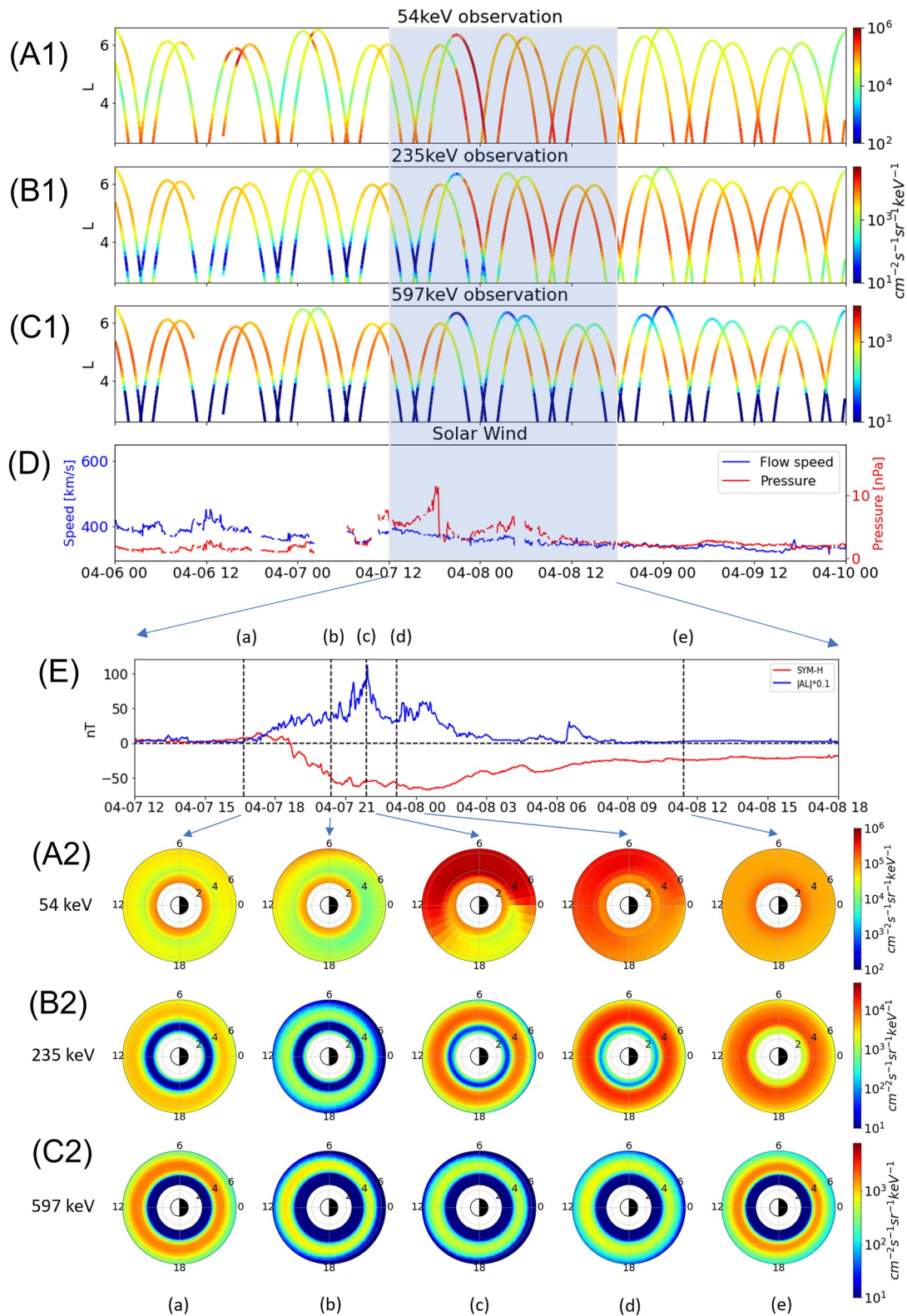
Figure 8. (A1-C1) Observations from 6th April 2016 to 10th April 2016 for 54 , 235 and 597 keV channel (d) Solar wind speed and pressure from OMNI (e) Selected range of SYM-H and AL (7th Arpil 2016/12:00–8th April 2016/18:00) (A2-C2) A series of panels showing the model reconstruction of the electron fluxes as a function of L-shell and MLT for different energy channels (54 keV, 235 keV, and 597 keV) at different snapshots in time: (a) 7th Arpil 2016/16:40, in the quiet period before the storm, (b) 7th Arpil 2016/20:25, during the main phase, (c) 7th Arpil 2016/21:55 the time of maximum |*AL*|, (d) 7th Arpil 2016/23:10, early recovery, and (e) 8th Arpil 2016/11:25, the late recovery period after the storm. The top panel shows the SYM-H and AL index during the course of the storm.
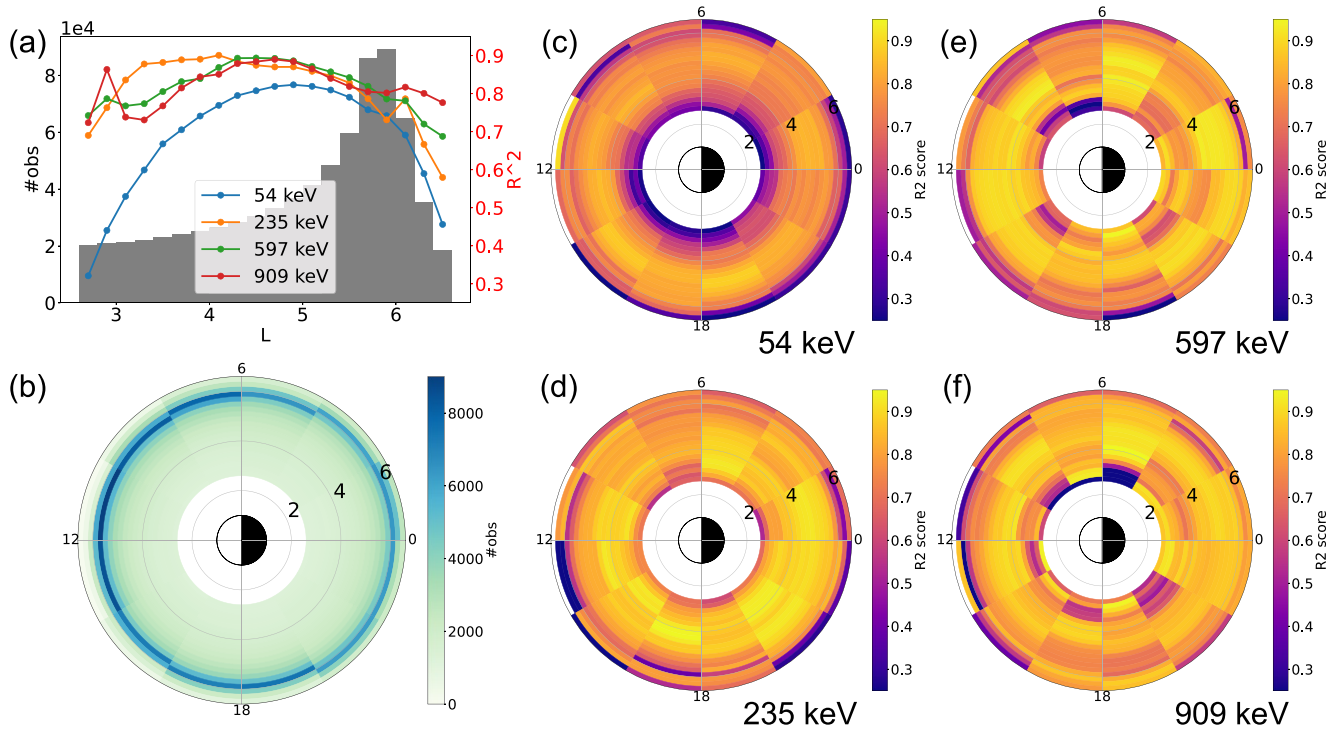
Figure 9. R2 score in the test data set. (a): R2 values of test datasets for different L shells. The background gray hist data shows all the data distribution along L shell of 54 keV channel. (b) The training data distribution of 54 keV. (c)–(f): The R2 values of test data set as function of L and MLT for different channels. The result includes 20 Lshell bins from $L = 2.6$ to $L = 6.6$ with $\Delta L = 0.2$ and 12 MLT bins with $\Delta MLT = 2$.

The results of localization to the dawnside of the Earth are consistent with a previous study of the same observation, a case study, and statistical distribution result (Allison et al., 2017; Zhao et al., 2017). In the early recovery phase of the storm (time d), the enhanced fluxes begin to diminish, and the distribution begins to take on a more MLT-symmetric structure. In the late recovery (time e), the electron distributions in all channels begin to relax back to their pre-storm values. The dropout process might result from the magnetopause shadowing as the dynamic pressure increases. It is interesting to note that the peak flux levels occur at increasingly later times, with increasing electron energies, which is consistent with previous observations (Thorne et al., 2013) and is likely related to the timescales of the local acceleration process. It is worth mentioning that the detailed physics of radiation belt dropouts is still an open problem which we do not aim to address in the present study. We can only speculate that since there was a dynamic pressure enhancement when the drop out happened, it is likely that magnetopause shadowing was the main loss process, but interpretation of this physics is not our focus.

Thus, Figures 8 and 9 show that the ORIENT-M model is able to reconstruct the dynamic evolution of electron fluxes at different energies and capture the L-shell and MLT dependence of both the lower energy fluxes as well as the higher energy fluxes, which is challenging to study using in-situ observations alone.

5. Summary

Here, we presented a set of Outer Radiation belt Electron Neural net model for Medium energy electrons (ORIENT-M). The ORIENT-M models are driven purely by a time history of geomagnetic indices and solar wind parameters, meaning that they do not need any other in situ data (e.g., fluxes from LEO satellites) to provide boundary conditions as inputs into the model, and thus our models are able to reconstruct energetic electron fluxes for periods deep in the past and into the future, as long as the geomagnetic indices and solar wind parameters are available. Our models are trained using six years of electron flux data from the MagEIS instrument onboard Van Allen Probes, and we have shown only four representative energy channels in this study. Any predictions of our models for periods in the past or the future are thus essentially a prediction of what the MagEIS instrument on Van Allen Probes should observe under the input conditions provided to the model at that time.

The model performance of the test data set (which was held out during model training), as well as for complete out-of-sample periods, that is, a geomagnetic storm in March 2017, was demonstrated and shows a high coefficient of determination ($R^2 \sim 0.7$–0.9). The model could reproduce the effects of particle acceleration, decay of the electron fluxes, and energy-dependent dynamics of electron fluxes in the radiation belt. Given its excellent performance in predicting low to high energy electron fluxes, our model was able to capture the MLT-dependent electron flux dynamics. We presented the MLT dependence during a geomagnetic storm that occurred on 8 April 2016. The timing and MLT differences of electron enhancement at 54 keV were well captured by the model, and hence the implication is that the model baked in all the relevant physical processes that shaped the resulting electron distribution. The electron flux asymmetry was seen to be much higher in the dawn sector and the eastward diffusion drift process was reflected in the model result.

The ORIENT-M model presented in this study represents a novel capability in modeling the subrelativistic (10–100s keV) electron flux population. At present, such electron fluxes are studied with either first-principles physics-based numerical modeling (Jordanova et al., 2010; Li et al., 2010), neither of which is able to capture the energy-dependent, dynamical variation of the global distribution of the observations. The present model is aimed at filling this important gap in our modeling capabilities and can be used as an important tool for both space weather (i.e., spacecraft charging) applications, as well as to discern the physical processes that control the dynamics of this key particle population.

Data Availability Statement

The data and model files are available at https://doi.org/10.5281/zenodo.6299967 and example code is available at https://github.com/donglai96/ORIENT-M.

References

Akiba, T., Sano, S., Yanase, T., Ohta, T., & Koyama, M. (2019). Optuna: A next-generation hyperparameter optimization framework. In *Proceedings of the 25th ACM SIGKDD international conference on knowledge discovery and data mining* (pp. 2623–2631).

Allison, H. J., Horne, R. B., Glauert, S. A., & Zanna, G. D. (2017). The magnetic local time distribution of energetic electrons in the radiation belt region. *Journal of Geophysical Research: Space Physics*, *122*(8), 8108–8123. https://doi.org/10.1002/2017ja024084

Baker, D. N., Erickson, P. J., Fennell, J. F., Foster, J. C., Jaynes, A. N., & Verronen, P. T. (2017). Space weather effects in the Earth's radiation belts. *Space Science Reviews*, *214*(1), 17. https://doi.org/10.1007/s11214-017-0452-7

Baker, D. N., Higbie, P. R., Belian, R. D., & Hones, E. W. (1979). Do Jovian electrons influence the terrestrial outer radiation zone? *Geophysical Research Letters*, *6*(6), 531–534. https://doi.org/10.1029/gl006i006p00531

Baker, D. N., Jaynes, A. N., Hoxie, V. C., Thorne, R. M., Foster, J. C., Li, X., et al. (2014). An impenetrable barrier to ultrarelativistic electrons in the Van Allen radiation belts. *Nature*, *515*(7528), 531–534. https://doi.org/10.1038/nature13956

Balikhin, M. A., Boynton, R. J., Walker, S. N., Borovsky, J. E., Billings, S. A., & Wei, H. L. (2011). Using the NARMAX approach to model the evolution of energetic electrons fluxes at geostationary orbit. *Geophysical Research Letters*, *38*(18). https://doi.org/10.1029/2011gl048980

Bergstra, J., Bardenet, R., Bengio, Y., & Kégl, B. (2011). Algorithms for hyper-parameter optimization. *Advances in Neural Information Processing Systems*, *24*.

Bergstra, J., Yamins, D., & Cox, D. (2013). Making a science of model search: Hyperparameter optimization in hundreds of dimensions for vision architectures. In S. Dasgupta & D. McAllester (Eds.), *Proceedings of the 30th international conference on machine learning*, *Proceedings of machine learning Research* (Vol. 28, pp. 115–123). PMLR. Retrieved from https://proceedings.mlr.press/v28/bergstra13.html

Blake, J. B., Carranza, P. A., Claudepierre, S. G., Clemmons, J. H., Crain, W. R., Dotan, Y., et al. (2013). The magnetic electron Ion spectrometer (MagEIS) instruments aboard the radiation belt storm probes (RBSP) spacecraft. *Space Science Reviews*, *179*(1–4), 383–421. https://doi.org/10.1007/s11214-013-9991-8

Bortnik, J., Chu, X., Ma, Q., Li, W., Zhang, X., Thorne, R. M., et al. (2018). Chapter 11 - Artificial neural networks for determining magnetospheric conditions. In E. Camporeale, S. Wing, & J. R. Johnson (Eds.), *Machine learning techniques for space weather* (pp. 279–300). Elsevier. Retrieved from https://www.sciencedirect.com/science/article/pii/B9780128117880000111

Bortnik, J., Li, W., Thorne, R. M., & Angelopoulos, V. (2016). A unified approach to inner magnetospheric state prediction. *Journal of Geophysical Research: Space Physics*, *121*(3), 2423–2430. https://doi.org/10.1002/2015ja021733

Bortnik, J., & Thorne, R. (2007). The dual role of ELF/VLF chorus waves in the acceleration and precipitation of radiation belt electrons. *Journal of Atmospheric and Solar-Terrestrial Physics*, *69*(3), 378–386. https://doi.org/10.1016/j.jastp.2006.05.030

Brautigam, D., & Bell, J. (1995). Crresele documentation. Interim scientific report.

Chu, X., Bortnik, J., Li, W., Ma, Q., Angelopoulos, V., & Thorne, R. M. (2017). Erosion and refilling of the plasmasphere during a geomagnetic storm modeled by a neural network. *Journal of Geophysical Research: Space Physics*, *122*(7), 7118–7129. https://doi.org/10.1002/2017ja023948

Chu, X., Bortnik, J., Li, W., Ma, Q., Denton, R., Yue, C., et al. (2017). A neural network model of three-dimensional dynamic electron density in the inner magnetosphere. *Journal of Geophysical Research: Space Physics*, *122*(9), 9183–9197. https://doi.org/10.1002/2017ja024464

Chu, X., Ma, D., Bortnik, J., Tobiska, W. K., Cruz, A., Bouwer, S. D., et al. (2021). Relativistic electron model in the outer radiation belt using a neural network approach. *Space Weather*, *19*(12), e2021SW002808. https://doi.org/10.1029/2021SW002808

Claudepierre, S. G., Ma, Q., Bortnik, J., O'Brien, T. P., Fennell, J. F., & Blake, J. B. (2020a). Empirically estimated electron lifetimes in the Earth's radiation belts: Comparison with theory. *Geophysical Research Letters*, *47*(3), e2019GL086056. https://doi.org/10.1029/2019gl086056

Claudepierre, S. G., Ma, Q., Bortnik, J., O'Brien, T. P., Fennell, J. F., & Blake, J. B. (2020b). Empirically estimated electron lifetimes in the Earth's radiation belts: Van Allen probe observations. *Geophysical Research Letters*, *47*(3), e2019GL086053. https://doi.org/10.1029/2019gl086053

Claudepierre, S. G., & O'Brien, T. P. (2020). Specifying high-altitude electrons using low-altitude LEO systems: The SHELLS model. *Space Weather*, *18*(3). https://doi.org/10.1029/2019sw002402

Claudepierre, S. G., O'Brien, T. P., Blake, J. B., Fennell, J. F., Roeder, J. L., Clemmons, J. H., et al. (2015). A background correction algorithm for Van Allen Probes MagEIS electron flux measurements. *Journal of Geophysical Research: Space Physics*, *120*(7), 5703–5727. https://doi.org/10.1002/2015ja021171

Claudepierre, S. G., O'Brien, T. P., Looper, M. D., Blake, J. B., Fennell, J. F., Roeder, J. L., et al. (2019). A revised look at relativistic electrons in the Earth's inner radiation zone and slot region. *Journal of Geophysical Research: Space Physics*, *124*(2), 934–951. https://doi.org/10.1029/2018ja026349

Ginet, G. P., O'Brien, T. P., Huston, S. L., Johnston, W. R., Guild, T. B., Friedel, R., et al. (2013). AE9, AP9 and SPM: New models for specifying the trapped energetic particle and space plasma environment. *Space Science Reviews*, *179*(1–4), 579–615. https://doi.org/10.1007/s11214-013-9964-y

Glauert, S. A., Horne, R. B., & Meredith, N. P. (2014). Three-dimensional electron radiation belt simulations using the bas radiation belt model with new diffusion models for chorus, plasmaspheric hiss, and lightning-generated whistlers. *Journal of Geophysical Research: Space Physics*, *119*(1), 268–289. https://doi.org/10.1002/2013JA019281

Hands, A., Ryden, K., Underwood, C., Rodgers, D., & Evans, H. (2015). A new model of outer belt electrons for dielectric internal charging (MOBE-DIC). *IEEE Transactions on Nuclear Science*, *62*(6), 2767–2775. https://doi.org/10.1109/tns.2015.2475134

Horne, R. B., Glauert, S. A., & Thorne, R. M. (2003). Resonant diffusion of radiation belt electrons by whistler-mode chorus. *Geophysical Research Letters*, *30*(9), 1493. https://doi.org/10.1029/2003GL016963

Ioffe, S., & Szegedy, C. (2015). Batch normalization: Accelerating deep network training by reducing internal covariate shift. In *International conference on machine learning* (pp. 448–456).

Jaynes, A. N., Baker, D. N., Singer, H. J., Rodriguez, J. V., Loto'aniu, T. M., Ali, A. F., et al. (2015). Source and seed populations for relativistic electrons: Their roles in radiation belt changes. *Journal of Geophysical Research: Space Physics*, *120*(9), 7240–7254. https://doi.org/10.1002/2015ja021234

Jordanova, V. K., Thorne, R. M., Li, W., & Miyoshi, Y. (2010). Excitation of whistler mode chorus from global ring current simulations. *Journal of Geophysical Research*, *115*(A5). https://doi.org/10.1029/2009JA014810

Kuhn, M., & Johnson, K. (2013). *Applied predictive modeling* (Vol. 26). Springer.

LeCun, Y., Bengio, Y., & Hinton, G. (2015). Deep learning. *Nature*, *521*(7553), 436–444. https://doi.org/10.1038/nature14539

Li, W., & Hudson, M. (2019). Earth's Van Allen radiation belts: From discovery to the Van Allen probes era. *Journal of Geophysical Research: Space Physics*, *124*(11), 8319–8351. https://doi.org/10.1029/2018ja025940

Li, W., Thorne, R. M., Ma, Q., Ni, B., Bortnik, J., Baker, D. N., et al. (2014). Radiation belt electron acceleration by chorus waves during the 17 March 2013 storm. *Journal of Geophysical Research: Space Physics*, *119*(6), 4681–4693. https://doi.org/10.1002/2014ja019945

Li, W., Thorne, R. M., Nishimura, Y., Bortnik, J., Angelopoulos, V., McFadden, J. P., et al. (2010). Themis analysis of observed equatorial electron distributions responsible for the chorus excitation. *Journal of Geophysical Research*, *115*(A6). https://doi.org/10.1029/2009JA014845

Li, X., Baker, D. N., O'Brien, T. P., Xie, L., & Zong, Q. G. (2006). Correlation between the inner edge of outer radiation belt electrons and the innermost plasmapause location. *Geophysical Research Letters*, *33*(14), L14107. https://doi.org/10.1029/2006gl026294

Li, X., Oh, K. S., & Temerin, M. (2007). Prediction of the al index using solar wind parameters. *Journal of Geophysical Research*, *112*(A6). https://doi.org/10.1029/2006JA011918

Lima, R. P. d., Chen, Y., & Lin, Y. (2020). Forecasting megaelectron-volt electrons inside Earth's outer radiation belt: PreMevE 2.0 based on supervised machine learning algorithms. *Space Weather*, *18*(2). https://doi.org/10.1029/2019sw002399

Luo, B., Li, X., Temerin, M., & Liu, S. (2013). Prediction of the au, al, and ae indices using solar wind parameters. *Journal of Geophysical Research: Space Physics*, *118*(12), 7683–7694. https://doi.org/10.1002/2013JA019188

Lyons, L., & Thorne, R. (1973). Equilibrium structure of radiation belt electrons. *Journal of Geophysical Research*, *78*(13), 2142–2149. https://doi.org/10.1029/ja078i013p02142

Ma, Q., Li, W., Thorne, R. M., Bortnik, J., Reeves, G. D., Kletzing, C. A., et al. (2016). Characteristic energy range of electron scattering due to plasmaspheric hiss. *Journal of Geophysical Research: Space Physics*, *121*(12), 11737–11749. https://doi.org/10.1002/2016ja023311

Ma, Q., Li, W., Thorne, R. M., Ni, B., Kletzing, C. A., Kurth, W. S., et al. (2015). Modeling inward diffusion and slow decay of energetic electrons in the Earth's outer radiation belt. *Geophysical Research Letters*, *42*(4), 987–995. https://doi.org/10.1002/2014gl062977

Mauk, B. H., Fox, N. J., Kanekal, S. G., Kessel, R. L., Sibeck, D. G., & Ukhorskiy, A. (2013). Science objectives and rationale for the radiation belt storm probes mission. *Space Science Reviews*, *179*(1–4), 3–27. https://doi.org/10.1007/s11214-012-9908-y

Nair, V., & Hinton, G. E. (2010). Rectified linear units improve restricted Boltzmann machines. In *Icml*.

Reeves, G. D., Chen, Y., Cunningham, G. S., Friedel, R. W. H., Henderson, M. G., Jordanova, V. K., et al. (2012a). Dynamic radiation environment assimilation model: Dream. *Space Weather*, *10*(3). https://doi.org/10.1029/2011sw000729

Reeves, G. D., Chen, Y., Cunningham, G. S., Friedel, R. W. H., Henderson, M. G., Jordanova, V. K., et al. (2012b). Dynamic radiation environment assimilation model: Dream. *Space Weather*, *10*(3). https://doi.org/10.1029/2011SW000729

Reeves, G. D., Friedel, R. H. W., Larsen, B. A., Skoug, R. M., Funsten, H. O., Claudepierre, S. G., et al. (2016). Energy-dependent dynamics of keV to MeV electrons in the inner zone, outer zone, and slot regions. *Journal of Geophysical Research: Space Physics*, *121*(1), 397–412. https://doi.org/10.1002/2015ja021569

Reeves, G. D., McAdams, K. L., Friedel, R. H. W., & O'Brien, T. P. (2003). Acceleration and loss of relativistic electrons during geomagnetic storms. *Geophysical Research Letters*, *30*(10). https://doi.org/10.1029/2002gl016513

Sawyer, D. M., & Vette, J. I. (1976). AP-8 trapped proton environment for solar maximum and solar minimum. *Nasa Sti/Recon Technical Report N*, *77*, 18983.

Sicard-Piet, A., Bourdarie, S., Boscher, D., & Friedel, R. (2006). A model for the geostationary electron environment: POLE, from 30 keV to 5.2 MeV. *IEEE Transactions on Nuclear Science*, *53*(4), 1844–1850. https://doi.org/10.1109/tns.2006.877878

Sicard-Piet, A., Bourdarie, S., Boscher, D., Friedel, R. H. W., Thomsen, M., Goka, T., et al. (2008). A new international geostationary electron model: IGE-2006, from 1 keV to 5.2 MeV. *Space Weather*, *6*(7). https://doi.org/10.1029/2007sw000368

Smirnov, A. G., Berrendorf, M., Shprits, Y. Y., Kronberg, E. A., Allison, H. J., Aseev, N. A., et al. (2020). Medium energy electron flux in Earth's outer radiation belt (merlin): A machine learning model. *Space Weather*, *18*(11). https://doi.org/10.1029/2020sw002532

Thorne, R. M. (2010). Radiation belt dynamics: The importance of wave-particle interactions. *Geophysical Research Letters*, *37*(22). https://doi.org/10.1029/2010GL044990

Thorne, R. M., Li, W., Ni, B., Ma, Q., Bortnik, J., Chen, L., et al. (2013). Rapid local acceleration of relativistic radiation-belt electrons by magnetospheric chorus. *Nature*, *504*(7480), 411–414. https://doi.org/10.1038/nature12889

Tu, W., Cunningham, G. S., Chen, Y., Henderson, M. G., Camporeale, E., & Reeves, G. D. (2013). Modeling radiation belt electron dynamics during GEM challenge intervals with the DREAM3D diffusion model. *Journal of Geophysical Research: Space Physics*, *118*(10), 6197–6211. https://doi.org/10.1002/jgra.50560

Turner, D. L., Angelopoulos, V., Li, W., Hartinger, M. D., Usanova, M., Mann, I. R., et al. (2013). On the storm-time evolution of relativistic electron phase space density in Earth's outer radiation belt. *Journal of Geophysical Research: Space Physics*, *118*(5), 2196–2212. https://doi.org/10.1002/jgra.50151

Van Allen, J. A., & Frank, L. A. (1959). Radiation around the Earth to a radial distance of 107, 400 km. *Nature*, *183*(4659), 430–434. https://doi.org/10.1038/183430a0

Van Allen, J. A., Ludwig, G. H., Ray, E. C., & Mcilwain, C. E. (1958). Observation of high intensity radiation by satellites 1958 alpha and gamma. *Journal of Jet Propulsion*, *28*(9), 588–592. https://doi.org/10.2514/8.7396

Walsh, B. M., Bhakyapaibul, T., & Zou, Y. (2019). Quantifying the uncertainty of using solar wind measurements for geospace inputs. *Journal of Geophysical Research: Space Physics*, *124*(5), 3291–3302. https://doi.org/10.1029/2019JA026507

Wing, S., Johnson, J. R., Camporeale, E., & Reeves, G. D. (2016). Information theoretical approach to discovering solar wind drivers of the outer radiation belt. *Journal of Geophysical Research: Space Physics*, *121*(10), 9378–9399. https://doi.org/10.1002/2016JA022711

Wing, S., Johnson, J. R., Turner, D. L., Ukhorskiy, A. Y., & Boyd, A. J. (2022). Untangling the solar wind and magnetospheric drivers of the radiation belt electrons. *Journal of Geophysical Research: Space Physics*, *127*(4), e2021JA030246. https://doi.org/10.1029/2021JA030246

Wrenn, G. L., Rodgers, D. J., & Buehler, P. (2000). Modeling the outer belt enhancements of penetrating electrons. *Journal of Spacecraft and Rockets*, *37*(3), 408–415. https://doi.org/10.2514/2.3575

Xiao, F., Su, Z., Zheng, H., & Wang, S. (2009). Modeling of outer radiation belt electrons by multidimensional diffusion process. *Journal of Geophysical Research*, *114*(A3). https://doi.org/10.1029/2008ja013580

Zhang, H., Fu, S., Xie, L., Zhao, D., Yue, C., Pu, Z., et al. (2020). Relativistic electron flux prediction at geosynchronous orbit based on the neural network and the quantile regression method. *Space Weather*, *18*(9). https://doi.org/10.1029/2020sw002445

Zhao, H., Baker, D. N., Califf, S., Li, X., Jaynes, A. N., Leonard, T., et al. (2017). Van allen probes measurements of energetic particle deep penetration into the low L region (L < 4) during the storm on 8 April 2016. *Journal of Geophysical Research: Space Physics*, *122*(12), 12140–12152. https://doi.org/10.1002/2017ja024558